DES-2016-0203
Fermilab-PUB-16-567-AE

MNRAS **000**, 1–18 (2016) Preprint 1 December 2016 Compiled using MNRAS LaTeX style file v3.0

Weak lensing magnification in the Dark Energy Survey Science Verification data

M. Garcia-Fernandez[1⋆], E. Sanchez[1], I. Sevilla-Noarbe[1], E. Suchyta[2], E. M. Huff[3], E. Gaztanaga[4], J. Aleksić[5], R. Ponce[1], F. J. Castander[4], B. Hoyle[6], T. M. C. Abbott[7], F. B. Abdalla[8,9], S. Allam[10], J. Annis[10], A. Benoit-Lévy[8,11,12], G. M. Bernstein[13], E. Bertin[11,12], D. Brooks[8], E. Buckley-Geer[10], D. L. Burke[14,15], A. Carnero Rosell[16,17], M. Carrasco Kind[18,19], J. Carretero[4,5], M. Crocce[4], C. E. Cunha[14], C. B. D'Andrea[20,21], L. N. da Costa[16,17], D. L. DePoy[22], S. Desai[23], H. T. Diehl[10], T. F. Eifler[3], A. E. Evrard[24,25], E. Fernandez[5], B. Flaugher[10], P. Fosalba[4], J. Frieman[10,26], J. García-Bellido[27], D. W. Gerdes[25], T. Giannantonio[28,29], D. Gruen[14,15], R. A. Gruendl[18,19], J. Gschwend[16,17], G. Gutierrez[10], D. J. James[7,30], M. Jarvis[13], D. Kirk[8], E. Krause[14], K. Kuehn[31], N. Kuropatkin[10], O. Lahav[8], M. Lima[16,32], N. MacCrann[33], M. A. G. Maia[16,17], M. March[13], J. L. Marshall[22], P. Melchior[34], R. Miquel[5,35], J. J. Mohr[36,37,38], A. A. Plazas[3], A. K. Romer[39], A. Roodman[14,15], E. S. Rykoff[14,15], V. Scarpine[10], M. Schubnell[25], R. C. Smith[7], M. Soares-Santos[10], F. Sobreira[16,40], G. Tarle[25], D. Thomas[20], A. R. Walker[7], W. Wester[10]

(The DES Collaboration)

Author affiliations are listed at the end of this paper.

Accepted XXX. Received YYY; in original form ZZZ

arXiv:1611.10326v1 [astro-ph.CO] 30 Nov 2016

ABSTRACT

In this paper the effect of weak lensing magnification on galaxy number counts is studied by cross-correlating the positions of two galaxy samples, separated by redshift, using data from the Dark Energy Survey Science Verification dataset. The analysis is carried out for two photometrically-selected galaxy samples, with mean photometric redshifts in the $0.2 < z < 0.4$ and $0.7 < z < 1.0$ ranges, in the *riz* bands. A signal is detected with a 3.5σ significance level in each of the bands tested, and is compatible with the magnification predicted by the ΛCDM model. After an extensive analysis, it cannot be attributed to any known systematic effect. The detection of the magnification signal is robust to estimated uncertainties in the outlier rate of the photometric redshifts, but this will be an important issue for use of photometric redshifts in magnification mesurements from larger samples. In addition to the detection of the magnification signal, a method to select the sample with the maximum signal-to-noise is proposed and validated with data.

Key words: methods: data analysis – techniques: photometric – gravitational lensing: weak – large-scale structure of the Universe

1 INTRODUCTION

Weak gravitational lensing of distant objects by the nearby large-scale structure of the Universe is a powerful probe of cosmology (Bartelmann & Schneider (2001); Meylan et al. (2006); Hoekstra & Jain (2008); van Waerbeke et al. (2010); Weinberg et al. (2013); Kilbinger (2015)) with two main signatures: magnification and shear.

Magnification is due to the convergent gravitational bending of the light emitted by distant sources by the matter located between those sources and the observer (Blandford et al. 1989). This leads to an isotropic observed size enlargement of the object while the surface brightness is conserved (Blandford & Narayan 1992), modifying three observed properties of the sources: size, magnitude and spatial density. The change of spatial density of galaxies due to gravitational lensing is known as number count magnification and is due to the increase of the observed flux

⋆ manuel.garcia-fernandez@ciemat.es

© 2016 The Authors

of the background galaxies, allowing the detection of objects that, in the absence of lensing, would be beyond the detection threshold (Bartelmann 1992b). Magnification is strongly dependent on the mass of the dark matter content along the line of sight to the source (Bartelmann (1992a); Bartelmann (1992c); Bartelmann (1995b); Bartelmann & Narayan (1995)). Therefore, its effect is not homogeneous and is spatially correlated with the location of lens galaxies and clusters, which are biased tracers of the dark matter field (White & Rees (1978); Kaiser (1984)).

Since magnification and shear are complementary effects of the same physical phenomenon, they depend on the same cosmological parameters, but in a slightly different manner. Thus, some degeneracies are broken on parameter constraints (e.g. at the $\Omega_M - \sigma_8$ plane) when combining magnification with shear-shear correlations (van Waerbeke 2010). Nevertheless, the major power of the combination of both methods is that they are sensitive to different sources of systematic errors. For example, number count magnification is independent from those systematic effects caused by shape determination. This constitutes a powerful feature that can be exploited to minimize systematic effects on a possible combination of magnification with galaxy-shear (gg-lensing) since both measurements are produced by the convergence field.

Extensive wide-field programs have allowed accurate measurements of weak lensing effects. However, magnification has been little studied due to its lower signal-to-noise. Previous measurements involve the use of very massive objects as lenses, such as luminous red galaxies (LRGs) and clusters (Broadhurst (1995); Bauer et al. (2014); Ford et al. (2014); Chiu et al. (2016)), or high redshift objects as sources, such as Lyman break galaxies (LBGs; Morrison et al. (2012)) and quasars (Seldner & Peebles (1979); Hogan et al. (1989); Fugmann (1990); Bartelmann & Schneider (1993); Ménard & Bartelmann (2002); Gaztañaga (2003); Scranton et al. (2005)) to improve signal-to-noise ratio. In addition to the number count technique used in this paper, other observational effects produced by magnification have been measured as well: the shift in magnitude (Ménard et al. 2010), flux (Jain & Lima 2011) and size (Huff & Graves 2014).

In this paper, the first detection of a magnification signal using photometric redshifts for the general galaxy population is shown using the Dark Energy Survey[1] Science Verification data. In addition to the detection of the measured signal, a thorough analysis of the potential sources of systematic errors is made.

The structure of the paper is as follows: in section 2 the theory behind magnification is summarized. The steps leading to a detection are described in section 3, and section 4 describes the data sample. The methodology is validated in section 5 with a study on N-body simulations. The analysis of the data sample is made in section 6, concluding in section 7.

[1] www.darkenergysurvey.org

2 NUMBER COUNT MAGNIFICATION

Number count magnification can be detected and quantified by the deviation of the expected object counts in the positional correlation of a foreground and a background galaxy sample (Seldner & Peebles 1979). These galaxy samples, in absence of magnification, are uncorrelated if their redshift distributions have a negligible overlap. In this section, the formalism that will quantify its effect on this observable is presented.

The observed two-point angular cross-correlation function between the i- and j-th redshift bins, including magnification, is defined as (Bartelmann 1995a)

$$\omega_{ij}(\theta) = \langle \delta_O(\hat{\boldsymbol{n}}, z_i, f_i)\delta_O(\hat{\boldsymbol{n}}', z_j, f_j)\rangle_\theta, \tag{1}$$

where θ is the angle subtended by the two direction vectors $\hat{\boldsymbol{n}}, \hat{\boldsymbol{n}}'$ and the observed density contrast (δ_O) is

$$\delta_O(\hat{\boldsymbol{n}}, z_i, f_i) = \delta_g(\hat{\boldsymbol{n}}, z_i) + \delta_\mu(\hat{\boldsymbol{n}}, z_i, f_i); \tag{2}$$

where δ_g describes the fluctuations due to the intrinsic matter clustering at redshift z_i and δ_μ incorporates the fluctuations from magnification effects at a flux cut f_i.

The galaxy density contrast in the linear bias approximation is (Peacock & Dodds (1994); Clerkin et al. (2015))

$$\delta_g(\hat{\boldsymbol{n}}, z_i) = b_i \delta_M(\hat{\boldsymbol{n}}, z_i) \tag{3}$$

with b_i the galaxy-bias at redshift z_i and δ_M the intrinsic matter density contrast.

Following the approach used by Bartelmann & Schneider (2001) and Ménard et al. (2003), the magnification density contrast on the sky in direction $\hat{\boldsymbol{n}}$ is defined as

$$\delta_\mu(\hat{\boldsymbol{n}}, z, f_\mu) = \frac{N_\mu(\hat{\boldsymbol{n}}, z, f_\mu)}{N_0(\hat{\boldsymbol{n}}, z, f_0)} - 1. \tag{4}$$

Here $N_0(\hat{\boldsymbol{n}}, z, f_0)$ is the unlensed cumulative number count of sources located at redshift z, that is, the number of sources with observed flux greater than the threshold f_0, while, $N_\mu(\hat{\boldsymbol{n}}, z, f_\mu)$ is the lensed cumulative number count, affected by magnification.

Magnification by gravitational lenses increases the observed flux of background galaxies allowing one to see fainter sources changing the effective flux cut from f_0 to $f_\mu = f_0/\mu$. At the same time it stretches the solid angle behind the lenses, reducing the surface density of sources down to $N_\mu = N_0/\mu$ (Narayan 1989). Thus the density contrast may be rewritten as

$$\delta_\mu(\hat{\boldsymbol{n}}, z, f_\mu) = \frac{N_\mu(\hat{\boldsymbol{n}}, z, f_\mu)}{\mu N_\mu(\hat{\boldsymbol{n}}, z, \mu f_\mu)} - 1. \tag{5}$$

The cumulative number count can be locally parametrized as

$$N_\mu(\hat{\boldsymbol{n}}, z, f_\mu) = A\left(\frac{f_\mu}{f_*}\right)^{\alpha(f_\mu)} \tag{6}$$

where A, f_* are constant parameters and $\alpha(f_\mu)$ is a function of the flux limit. Substituting this parametrization into Equation 5:

$$\delta_\mu(\hat{\boldsymbol{n}}, z, f_\mu) = \mu^{-\alpha(f_\mu)-1} - 1. \tag{7}$$

Taking the weak lensing approximation, $\mu \simeq 1 + 2\kappa$ with $\kappa \ll 1$, where κ corresponds to the lensing convergence of

the field (Bartelmann & Schneider 1992), and converting from fluxes to magnitudes, the previous equation becomes (Narayan & Wallington 1993)

$$\delta_\mu(\hat{\boldsymbol{n}}, z, m) = 2\kappa(\hat{\boldsymbol{n}}, z)\,[\alpha(m) - 1] \tag{8}$$

with

$$\alpha(m) = 2.5\frac{d}{dm}[\log N_\mu(m)]. \tag{9}$$

The convergence κ is defined as (Blandford & Narayan (1992); Bartelmann & Schneider (2001))

$$\kappa(\hat{\boldsymbol{n}}, z) = \int_0^z dz' \frac{r(z')[r(z) - r(z')]}{r(z)} \nabla_\perp^2 \Phi[r(z'), \hat{\boldsymbol{n}}], \tag{10}$$

where $r(z)$ is the radial comoving distance at redshift z, $\nabla_\perp^2$ is the Laplacian on the coordinates of the plane transverse to the line of sight and Φ is the gravitational potential. Assuming that the gravitational potential and the matter density may be written as the sum of an homogeneous term plus a perturbation ($\Phi = \bar{\Phi} + \delta_\Phi$ and $\rho = \bar{\rho} + \delta_M$ respectively) the Poisson equation can be written as:

$$\nabla^2\Phi(r, \hat{\boldsymbol{n}}) = \nabla^2\delta_\Phi(r, \hat{\boldsymbol{n}}) = 4\pi G a^2 \bar{\rho}\delta_M(r, \hat{\boldsymbol{n}}), \tag{11}$$

where $a = 1/(1+z)$ is the scale factor. Expressing the matter density as a function of the critical matter density at present, this leads to (Grossman & Narayan 1989)

$$\nabla_\perp^2\Phi(r, \hat{\boldsymbol{n}}) = \frac{3H_0^2}{2ac^2}\Omega_M^0\delta_M(r, \hat{\boldsymbol{n}}), \tag{12}$$

with δ_g the galaxy density contrast, H_0 the Hubble constant and c the speed of light.

Combining Equations 2, 3 and 8 it is straightforward to arrive at (Hui et al. (2007); LoVerde et al. (2008); Hui et al. (2008)):

$$\begin{aligned}
\omega_{ij}(\theta) = \quad & \langle b_i b_j \delta_M(\hat{\boldsymbol{n}}, z_i)\delta_M(\hat{\boldsymbol{n}}', z_j)\rangle_\theta && \text{(13a)}\\
+ \quad & \langle b_i \delta_M(\hat{\boldsymbol{n}}, z_i)\delta_\mu(\hat{\boldsymbol{n}}', z_j, m_j)\rangle_\theta && \text{(13b)}\\
+ \quad & \langle b_j \delta_M(\hat{\boldsymbol{n}}', z_j)\delta_\mu(\hat{\boldsymbol{n}}, z_i, m_i)\rangle_\theta && \text{(13c)}\\
+ \quad & \langle \delta_\mu(\hat{\boldsymbol{n}}, z_i, m_i)\delta_\mu(\hat{\boldsymbol{n}}', z_j, m_j)\rangle_\theta. && \text{(13d)}
\end{aligned}$$

If it is assumed that $z_i < z_j$ where z_i are the lens redshift bins and z_j the source redshift bins, the only term that is non-vanishing, assuming well determined redshifts, are Equations 13b and 13d, where the last term is subleading, resulting (Ménard et al. 2003):

$$\begin{aligned}
\omega_{ij}(\theta) = \quad & b_i[\alpha(m_j) - 1]\tfrac{3H_0^2\Omega_M^0}{c^2} \\
\times \quad & \int_0^\infty dz_i' \tfrac{\phi_i(z_i')}{1+z_i'} \int_{z_i'}^\infty dz_j' \phi_j(z_j') \tfrac{r(z_i')[r(z_j') - r(z_i')]}{r(z_j')} \\
\times \quad & \int_0^\infty \tfrac{dkk}{2\pi} P_M(k, z_i') J_0(k\theta r(z_i')),
\end{aligned} \tag{14}$$

where P_M is the matter power spectrum, J_0 is zero-th order Bessel function and ϕ_i, ϕ_j are the redshift distribution of the lens and source sample respectively. A short-hand way to express the two point angular cross-correlation function due to magnification between a lens sample (L) and a source sample (S) with magnitude cut m_j is

$$\omega_{LS_j}(\theta) = b_L[\alpha_S(m_j) - 1]\omega_0(\theta). \tag{15}$$

Here b_L is the galaxy-bias of the lenses, $\alpha_S(m_j)$ the number count slope of the sources given by Equation 9 and $\omega_0(\theta)$ is the angular correlation function of the projected mass on the lens plane, whose dependence is only on the cosmology. The number count slope is evaluated at the threshold magnitude m_j, that is, the upper magnitude cut imposed on the j-th source sample.

3 MEASURING MAGNIFICATION THROUGH NUMBER COUNT

By inspection of Equations 9 and 15 and the gravitational lens equation (Blandford & Narayan 1992), three key properties can be deduced that are intrinsic to magnification:

- A non-zero two-point angular cross-correlation ω_{LS_j} appears between two galaxy samples at redshifts $z_{S_j} > z_L$ for those cases in which the slope $\alpha_S(m_j) \neq 1$ (magnification signal hereafter).
- The amplitude of the magnification signal evolves with the slope of the faint end of the number count distribution of the source sample and, assuming a Schechter (1976) luminosity function, eventually it reaches zero and becomes negative.
- For a given value of the number count slope, the signal strength is independent of the photometric band used (i.e. it is achromatic).

The steps towards a measurement of magnification via the number count technique in a photometric survey can be summarized as follows:

(i) Split the data sample into two well-separated photo-z bins, termed lens and source. Splitting must be done minimizing the overlap between the true redshift distributions of the samples. Otherwise, by Equation 13a, an additive signal is introduced.

(ii) For each photometric band, define several subsamples from the source sample using different values for the maximum (threshold) magnitude. This is made in order to trace the evolution of the amplitude of the magnification signal with the number count slope (see Equation 9).

(iii) Compute the two-point angular cross-correlation function between the unique common lens sample and each source subsample for each band.

Once the two-point angular correlation function has been measured, it can be compared with theoretical predictions as described in section 2 allowing the desired parameter constraints or the determination of the galaxy-bias of the lenses.

As has been stated previously, the amplitude of the measured cross-correlation function depends on the shape of the galaxy number count distribution. Nevertheless, due to this shape –for a fixed footprint population of galaxies and redshift distribution–, the brighter is the magnitude limit of the sample, the bigger is the amplitude of the two point angular cross correlation function. However, the number of bright galaxies is lower than the number of faint galaxies (Schechter 1976), so shot noise is bigger at brighter magnitude cuts, increasing their measurement uncertainties. For this reason, there exists a magnitude cut that is a trade-off between amplitude and shot noise, maximizing the signal-to-noise ratio. In order to find the optimum magnitude cut for a given sample, define the signal-to-noise ratio for a given

angular range and magnitude cut $m' < m$ as (Moessner & Jain 1998):

$$\frac{S}{N}(m) = \frac{\langle \omega_{LS}(\theta; m) \rangle}{\langle s(\omega_{LS}(\theta; m)) \rangle}, \tag{16}$$

where $\langle s(\omega_{LS}(\theta; m)) \rangle$ is the average shot noise of the two point angular cross correlation functions and the averages are extended to the angular range considered in the analysis. The shot noise for a given angular aperture is given by the number of pairs inside each angular bin as

$$\sigma(\omega_{LS}(\theta; m)) = \frac{1}{\sqrt{P_{LS}(\theta; m)}}, \tag{17}$$

where $P_{LS}(\theta; m)$ is the number of pairs from the lens-source samples separated by an angular distance θ for a magnitude cut $m' < m$. The number of pairs per angular bin is given by the product of the number of source galaxies that fall inside a given annulus times the number of sources inside that annulus. Considering, as a first order approach, that the samples are uniform, the number of lens-source pair-counts of galaxies for a bin centered at θ with solid angle Δ_Ω is given by

$$P_{LS}(\theta; m) = \left[\frac{N_L}{A}\Delta_\Omega(\theta)\right]\left[\frac{N_S(m)}{A}\Delta_\Omega(\theta)\right]. \tag{18}$$

Here A is the solid angle subtended by the dataset, N_L is the number of objects at the lens sample and $N_S(m)$ the number of objects on the source sample with magnitude limit m. Combining Equations 15, 16 and 18, results finally in

$$\frac{S}{N}(m) = \langle \omega_0 \rangle [\alpha(m) - 1] b_L \frac{\Omega}{A}\sqrt{N_L N_S(m)}, \tag{19}$$

where Ω is the solid angle subtended by an annulus with edges the maximum and minimum scales considered. Thus, for a sample, given size, magnitude and redshift distributions –assuming a cosmology– the signal-to-noise ratio can be estimated. Nevertheless, Equation 19 assumes that the angular bins are uncorrelated and should be taken as an upper bound to the signal-to-noise. Although this expression does not take into account the full covariance, the behavior

$$\frac{S}{N} \sim [\alpha(m) - 1]\sqrt{N_S(m)}, \tag{20}$$

is independent of cosmological and covariance assumptions up to a constant factor, allowing us to use this expression for finding the optimal cut that maximizes the signal-to-noise ratio.

4 THE DATA SAMPLE

The Dark Energy Survey (DES; Flaugher (2005)) is a photometric galaxy survey that uses the Dark Energy Camera (DECam; Diehl (2012); Flaugher et al. (2015)), mounted at the Blanco Telescope, at the Cerro Tololo Interamerican Observatory. The survey will cover about 5000 deg^2 of the southern hemisphere, imaging around 3×10^8 galaxies in 5 broad-band filters ($grizY$) at limiting magnitudes $g < 24.6$, $r < 24.1$, $i < 24.3$, $z < 23.9$. The sample used in this analysis corresponds to the Science Verification (DES-SV) data, which contains several disconnected fields. From the DES SVA1-Gold[2] main galaxy catalog (Crocce et al. 2016), the largest contiguous field is selected, the SPT-E. Regions with declination $< -61°$ are removed in order to avoid the Large Magellanic Cloud. MODEST_CLASS is employed as star-galaxy classifier (Chang et al. 2015).

The following color cuts are made in order to remove outliers in color space:

- $-1 < g - r < 3$,
- $-1 < r - i < 2$,
- $-1 < i - z < 2$;

where g, r, i, z stand for the corresponding MAG_AUTO magnitude measured by SExtractor (Bertin & Arnouts 1996).

Regions of the sky that are tagged as bad, amounting to four per cent of the total area, are removed. An area of radius 2 arcminutes around each 2MASS star is masked to avoid stellar halos (Mandelbaum et al. (2005); Scranton et al. (2005)).

The DES Data Management (Sevilla et al. (2011); Desai et al. (2012); Mohr et al. (2012)) produces a MANGLE[3] (Swanson et al. 2008) magnitude limit mask that is later translated to a $N_{\rm side} = 4096$ HEALPix[4] (Górski et al. 2005) mask. Since the HEALPix mask is a division of the celestial sphere with romboid-like shaped pixels with the same area, to avoid boundary effects due to the possible mismatch between the MANGLE and HEALPix masks, each pixel is required to be totally inside the observed footprint as determined by MANGLE, by demanding

- $r_{\rm fracdet} = 1$,
- $i_{\rm fracdet} = 1$,
- $z_{\rm fracdet} = 1$;

where $r_{\rm fracdet}, i_{\rm fracdet}, z_{\rm fracdet}$ is the fraction of the pixel lying inside the footprint for r, i, z bands respectively.

Depth cuts are also imposed on the riz-bands in order to have uniform depth when combined with the magnitude cuts. These depth cuts are reached by including only the regions that meet the following conditions:

- $r_{\rm lim} > 23.0$,
- $i_{\rm lim} > 22.5$,
- $z_{\rm lim} > 22.0$;

where $r_{\rm lim}, i_{\rm lim}, z_{\rm lim}$ stand for the magnitude limit in the corresponding band, that is, the faintest magnitude at which the flux of a galaxy is detected at 10σ significance level. The resulting footprint, as shown in Figure 1, after all the masking cuts amounts to 121 deg^2.

Photometric redshifts (photo-z) have been estimated using different techniques. In particular, the fiducial code used in this work employs a machine-learning algorithm (random forests) as implemented by TPZ (Carrasco Kind & Brunner 2013), which was shown to perform well on SV data (Sánchez et al. 2014). The redshifts of the galaxies are defined according to the mean of the probability density functions given by TPZ ($z_{\rm ph}$). Other methods are also employed to demonstrate that the measured two-point angular cross-correlation are not a feature induced by TPZ (see subsection 6.2).

[2] des.ncsa.illinois.edu/releases/SVA1

[3] http://space.mit.edu/~molly/mangle/

[4] healpix.jpl.nasa.gov

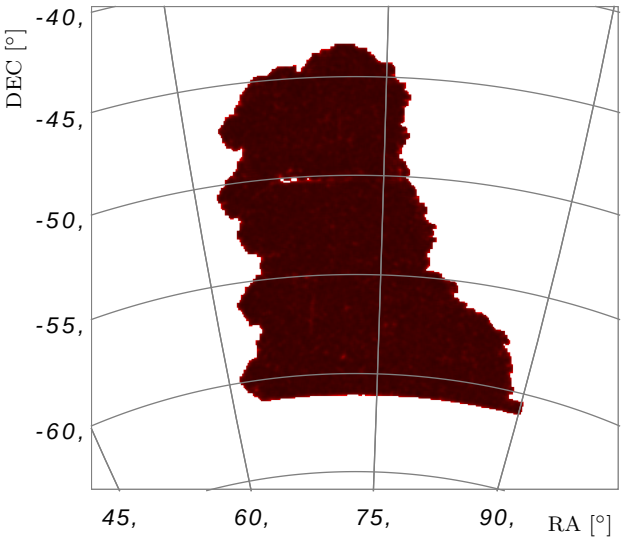

Figure 1. Final footprint of the DES SPT-E region after all masking is applied.

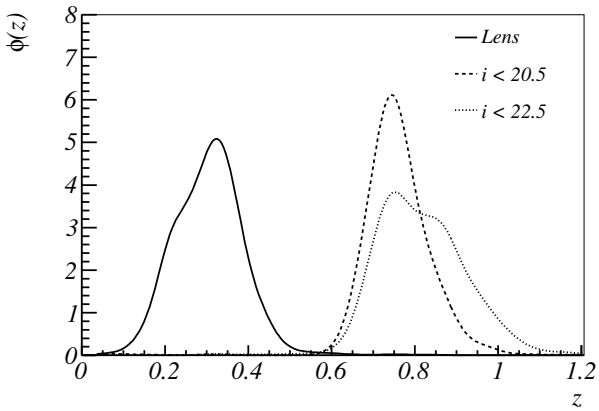

Figure 2. Redshift distributions from the stacking of the TPZ probability distribution functions for the lens and two i-band sub-samples of the source.

4.1 Lens sample

A unique lens sample is defined by the additional photo-z and magnitude cuts:

- $0.2 < z_{\rm ph} < 0.4$;
- $18.0 < i < 22.5$.

These requirements are imposed in order to be compatible with the first redshift bin of the so called 'benchmark sample' (Crocce et al. 2016). Note that the MAG_AUTO cut along with the previous i-band depth cut guarantees uniformity (Crocce et al. 2016).

4.2 Source sample

Three source samples are defined, one per band:

- R: $0.7 < z_{\rm ph} < 1.0$ and $r < 23.0$;
- I: $0.7 < z_{\rm ph} < 1.0$ and $i < 22.5$;
- Z: $0.7 < z_{\rm ph} < 1.0$ and $z < 22.0$.

Following the same approach we used on the lens, defined over the 'benchmark' sample, the MAG_AUTO cut along with the previously defined depth cuts also guarantee uniformity on the corresponding band.

Within each R, I, Z source sample five sub-samples that map the magnitude evolution are defined,

- R_1: $r < 21.0$; R_2: $r < 21.5$; R_3: $r < 22.0$; R_4: $r < 22.5$; R_5: $r < 23.0$.
- I_1: $i < 20.5$; I_2: $i < 21.0$; I_3: $i < 21.5$; I_4: $i < 22.0$; I_5: $i < 22.5$.
- Z_1: $z < 20.0$; Z_2: $z < 20.5$; Z_3: $z < 21.0$; Z_4: $z < 21.5$; Z_5: $z < 22.0$.

Here $\mathrm{S_j}$ with $\mathrm{j} = 1, 2, 3, 4, 5$ are the sub-samples of sample S with $\mathrm{S} \in \{\mathrm{R}, \mathrm{I}, \mathrm{Z}\}$. In Figure 2, the redshift distributions of the lens and source sample are shown. Note that the sub-samples $\mathrm{R}_5, \mathrm{I}_5, \mathrm{Z}_5$ are equal to $\mathrm{R}, \mathrm{I}, \mathrm{Z}$ respectively.

The g-band is not used on this analysis because when the same approach is followed and a uniform sample is defined in that band, the number of galaxies of the lens and source samples decrease dramatically. This increases the shot noise preventing the measurement of number count magnification.

5 APPLICATION TO A SIMULATED GALAXY SURVEY

In order to test the methodology described above in a controlled environment, isolated from any source of systematic error, it is applied to a simulated galaxy sample, in particular MICECAT v1.0. This mock is the first catalog release of the N-body simulation MICE-GC[5] (Fosalba et al. (2015a); Fosalba et al. (2015b); Crocce et al. (2015)). It assumes a flat ΛCDM Universe with cosmological parameters $\Omega_M = 0.25, \Omega_b = 0.044, h = 0.7$ and $\sigma_8 = 0.8$, using a light-cone that spans one eighth of the celestial sphere. Another advantage of using these simulations is the possibility of studying specific systematic effects, as described in subsection 6.2.

Among other properties, MICE-GC provides lensed and unlensed coordinates, true redshift (including redshift space distortions) and DES-*griz* unlensed magnitudes for the simulated galaxies, along with convergence and shear. Conversion from unlensed magnitudes to lensed magnitudes can be done by applying $m_\mu = m_0 - 2.5\log_{10}(1 + 2\kappa)$.

Having two sets of coordinates and magnitudes, one in a 'universe' with magnification and another without magnification, allows us to follow the methodology described in section 3 for both cases, serving as a test-bench in which it can be validated whether the presence of magnification in conditions similar to those of our survey can be discriminated and the sensitivity of the method to the magnification effect can be tested. In order to have a fiducial function with as little statistical uncertainty as possible, the full 5000 deg^2 of the MICE simulation are used. To match as much as possible the conditions of the DES-SV data, the same magnitude

[5] www.ice.cat/mice

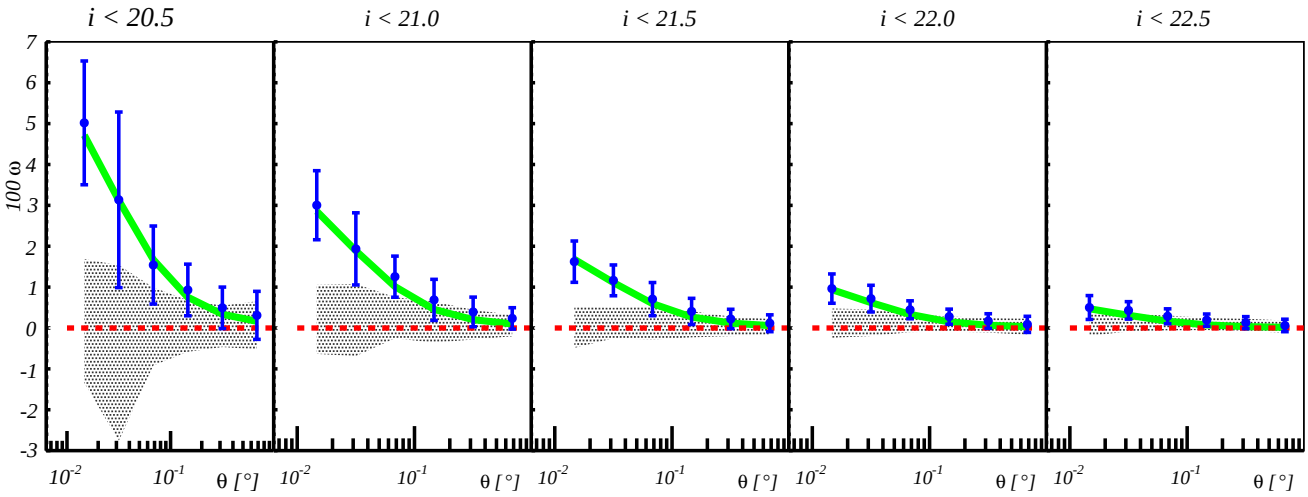

Figure 3. Two-point angular cross-correlation functions for the MICE simulation: measured, both with magnification (blue dots) and without (gray shade), versus that expected from weak lensing theory, both with magnification (green solid line) and without (red dashed line), the latter being zero.

cuts as those described in section 4 are applied to the lens and source samples. The covariance matrices used are the same as the ones used in section 6 in order to match the errors in the SV data analysis.

In Figure 3, the results of the magnification analysis in the MICE simulation for the cases with and without magnification can be seen compared with the theoretical expectations. The methodology used in this work clearly allows us to distinguish both cases for a data-set similar to that of the DES-SV data. A good agreement between the measured two-point angular cross-correlation and weak lensing theory described in section 2 using MICE cosmological parameters and the number count slope measured following the same approach as on section 6 is found. Nevertheless, results obtained with the MICE simulation can not be directly extrapolated to SV data to estimate the expected significance because the density of galaxies on the simulation is a factor ~ 3 smaller than on the SV data. Also, the luminosity function of the simulation is slightly different from the DES data, which has a direct impact on the number count slope and, consequently, on the amplitude of the measured signal.

6 DATA ANALYSIS

The analysis of the SV data is described here, showing first the detection of the magnification signal followed by the study and correction of systematic effects.

6.1 Signal detection

From the theoretical predictions described in section 2, the cross-correlation functions are expected to be non-zero for angular scales $\theta \lesssim 0.1$ degrees. Nevertheless, given the size of the data sample described in section 4, shot noise is expected to dominate over the size of the signal for scales $\theta < 0.01$ degrees. Taking this into account, six logarithmic angular bins are made in the range $0.01^\circ < \theta < 1^\circ$.

To estimate the cross-correlation functions, the tree-code TreeCorr[6] (Jarvis et al. 2004) and the Landy-Szalay estimator (Landy & Szalay 1993) are used:

$$\omega_{\mathrm{LS_j}}(\theta) = \frac{D_{\mathrm{L}}D_{\mathrm{S_j}}(\theta) - D_{\mathrm{L}}R_{\mathrm{S_j}}(\theta) - D_{\mathrm{S_j}}R_{\mathrm{L}}(\theta)}{R_{\mathrm{L}}R_{\mathrm{S_j}}(\theta)} + 1, \quad (21)$$

where $D_{\mathrm{L}}D_{\mathrm{S_j}}(\theta)$ is the number of pairs from the lens data sample L and the source data sub-sample $\mathrm{S_j}$ separated by an angular distance θ and $D_{\mathrm{L}}R_{\mathrm{S_j}}(\theta)$, $D_{\mathrm{S_j}}R_{\mathrm{L}}(\theta)$, $R_{\mathrm{L}}R_{\mathrm{S_j}}(\theta)$ are the corresponding values for the lens-random, source-random and random-random combinations normalized by the total number of objects on each sample.

Catalogs produced by Balrog[7] (Suchyta et al. 2016) are used as random samples. The Balrog catalogs are DES-like catalogs, where no intrinsic magnification signal has been included. The Balrog software generates images of fake objects, all with zero convergence κ, that are embedded into the DES-SV coadd images (convolving the objects with the measured point spread function, and applying the measured photometric calibration). Then SExtractor was run on them, using the same DES Data Management configuration parameters used for the image processing. The positions for the simulated objects were generated randomly over the celestial sphere, meaning that these positions are intrinsically unclustered. Hence, the detected Balrog objects amount to a set of random points, which sample the survey detection probability. For a full description and an application to the same measurement as in Crocce et al. (2016) see Suchyta et al. (2016).

The same cuts and masking of the data sample (section 4) are also applied to the the Balrog sample. A re-weighting following a nearest-neighbors approach was applied to Balrog objects in order to follow the same mag-

[6] github.com/rmjarvis/TreeCorr
[7] github.com/emhuff/Balrog

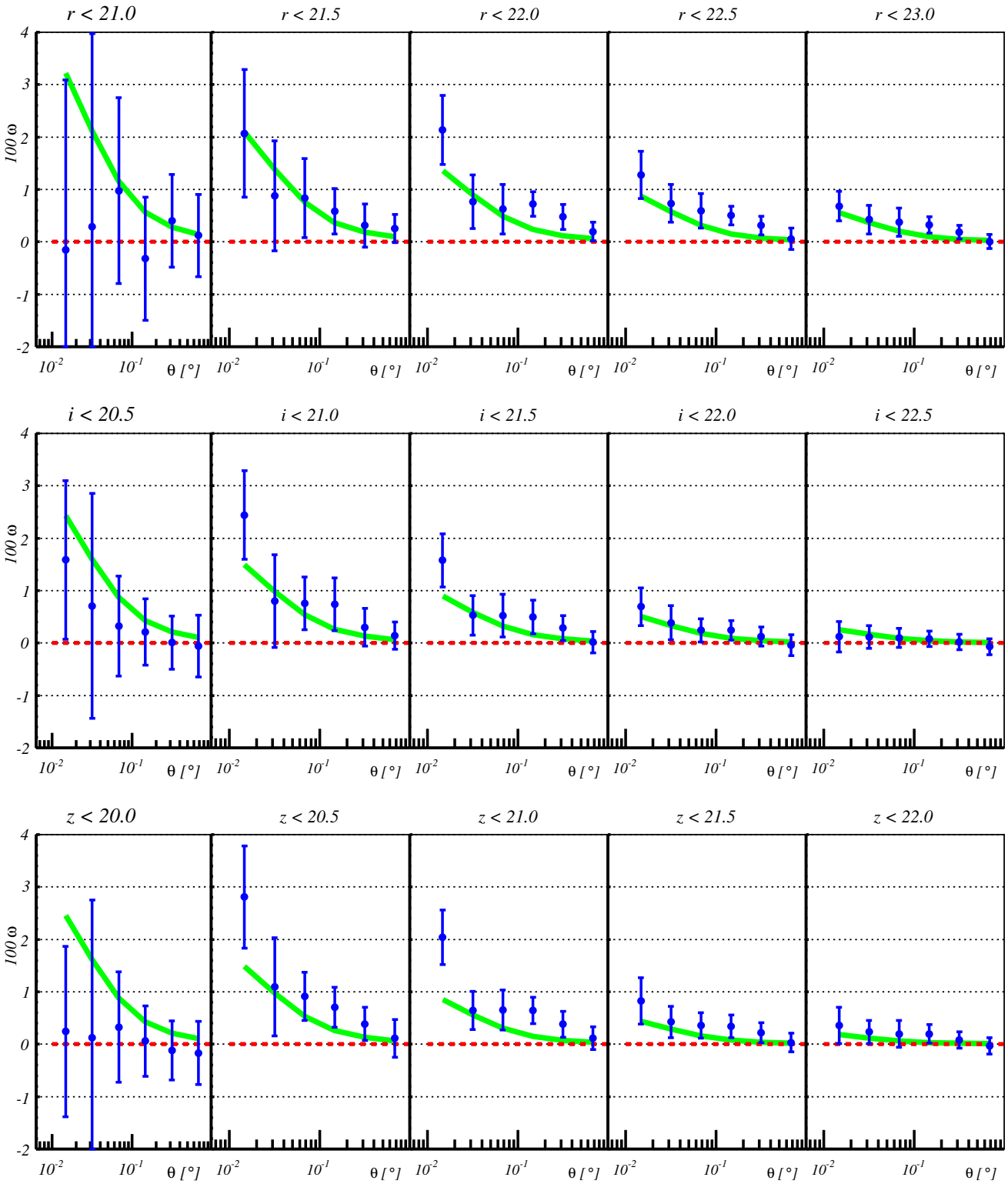

Figure 4. Measured cross-correlation functions of the lens sample with each source sample for the DES SVA1-Gold data using BALROG randoms. Each row corresponds to one of the R, I, Z source samples. Within each row, the sub-panels show the cross-correlation with the flux limited source sub-sample indicated above each. The green solid line shows the theoretical prediction using expression Equation 15 computed assuming a ΛCDM Cosmology (Planck Collaboration et al. 2015) and the previously measured galaxy-bias $b_{\rm L} = 1.07$ (Crocce et al. 2016). The red dashed line is an eye-guide for zero.

nitude distribution of the DES-SV data on both lens and sources.

The covariance matrix is computed for each band by jack-knife re-sampling the data

$$C_{\rm S}(\omega_{\rm LS_i}(\theta_\eta);\omega_{\rm LS_j}(\theta_\nu)) = \frac{N_{\rm JK}}{N_{\rm JK}-1} \times \sum_k^{N_{\rm JK}} [\omega^k_{\rm LS_i}(\theta_\eta) - \omega_{\rm LS_i}(\theta_\eta)][\omega^k_{\rm LS_j}(\theta_\nu) - \omega_{\rm LS_j}(\theta_\nu)], \quad (22)$$

where $\omega^k_{\rm LS_j}$ stands for the cross-correlation of the k-th jack-knife re-sample and $\omega_{\rm LS_j}$ is the cross-correlation of the full sample. The $N_{\rm JK} = 120$ jack-knife regions are defined by a k-means algorithm (MacQueen et al. 1967) using Python's machine learning library SCIKIT-LEARN[8] (Pedregosa et al. 2011). In order to get $N_{\rm JK}$ regions with equal area, the algorithm is trained on a uniform random sample following the footprint of the data demanding $N_{\rm JK}$ centers. The regions used on the re-sampling are composed by the Voronoi tessellation defined by these centers. These matrices trace the angular covariance as well as that between the correlation functions within each band. No covariance between bands is considered, since each band is treated independently on this work.

Measured two-point angular cross-correlation functions and standard weak lensing theoretical predictions can be found at Figure 4. Measured correlation functions are found to be non-zero, compatible with the weak lensing theory and its amplitude evolves with the magnitude cut. Nevertheless, no function with zero or negative amplitude is found. This is due to the magnitude cuts imposed to guarantee uniform depth that, for this data, defines only samples with positive values of the number count slope.

To compare with the expected theory, Equation 13b has been used assuming Planck Collaboration et al. (2015) cosmological parameteres. The bias of the lens sample $b_{\rm L} = 1.07$ is taken from Crocce et al. (2016) and is assumed to be a constant scale-independent parameter. The number count slope parameter $\alpha_{\rm S}$ is computed by fitting the cumulative number count of the sample S to a Schechter function (Schechter 1976) on the range of interest

$$N_\mu(m) = A\left[10^{0.4(m-m_*)}\right]^\beta \times \exp\left[-10^{0.4(m-m*)}\right], \quad (23)$$

where A, m_*, β are the parameters of the fit. Then $\alpha_{\rm S}(m)-1$ is computed by applying Equation 9 evaluating the derivative analytically, where $m_{\rm j}$ is the magnitude limit of the $\rm S_j$ sub-sample on the considered band. In Figure 5 the fit and the number count slope parameter for the I sample are shown. The use of this function here is only motivated because it is a good description of the points and is not intended to have any physical meaning.

An individual goodness of fit test of the measured two-point angular cross-correlation function comparing with the one expected from theory is made for each band:

$$\chi^2_{\rm Planck} = \sum_{\eta\nu ij} [\tilde{\omega}_{\rm LS_i}(\theta_\eta) - \omega_{\rm LS_i}(\theta_\eta)] \quad (24)$$

$$C^{-1}(\omega_{\rm LS_i}(\theta_\eta);\omega_{\rm LS_j}(\theta_\nu))[\tilde{\omega}_{\rm LS_j}(\theta_\nu) - \omega_{\rm LS_j}(\theta_\nu)], \quad (25)$$

[8] scikit-learn.org

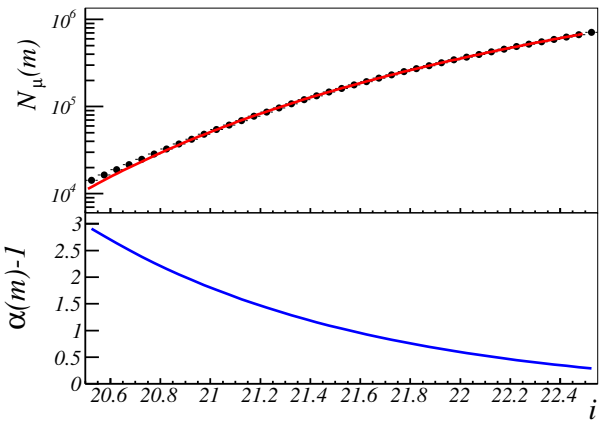

Figure 5. Top panel: Dots are the measured i-band cumulative number count as a function of the i-band magnitude. Red solid line is the fit using a Schechter function (see text). Bottom panel: number count slope $\alpha - 1$ measured from the fitted Schechter function of the top panel.

Band	$\chi^2_{\rm zero}/ndof$	$\chi^2_{\rm Planck}/ndof$	Significance
R	39.7/30	21.6/30	3.6σ
I	40.0/30	24.2/30	3.6σ
Z	53.5/30	37.9/30	3.5σ

Table 1. Significance of the detection of a magnification signal and χ^2 values. The χ^2 values are shown for the two hypothesis considered: the measurement is consistent with zero (absence of magnification) or the measured correlation functions are compatible with the theoretical predictions (see text).

where $\tilde{\omega}, \omega$ are the measured and theoretical cross-correlation functions respectively. Goodness of fit tests are also made testing the hypothesis of absence of magnification:

$$\chi^2_{\rm zero} = \sum_{\eta\nu ij} \tilde{\omega}_{\rm LS_i}(\theta_\eta) C^{-1}(\omega_{\rm LS_i}(\theta_\eta);\omega_{\rm LS_j}(\theta_\nu))\omega_{\rm LS_j}(\theta_\nu). \quad (26)$$

The χ^2 values can be seen in Table 1 showing good agreement (about 80 per cent) with the theoretical predictions described at section 2. Nevertheless, since in some cases magnification predicts the signal to be zero, to test which hypothesis is favored, the Bayes factor is used:

$$\mathcal{K} = \frac{P(M|\Theta)}{P(Z|\Theta)} = \frac{P(\Theta|M)}{P(\Theta|Z)}\frac{P(M)}{P(Z)}, \quad (27)$$

where

$$P(M|\Theta) = e^{-\chi^2_{\rm Planck}/2} \quad (28)$$

and

$$P(Z|\Theta) = e^{-\chi^2_{\rm zero}/2}. \quad (29)$$

The assumed prior sets detection and non-detection of magnification to be equally probable: $P(M) = P(Z)$. Significances through the the Bayes factor are computed for each function individually as well as for each band using the full covariance.

The significance for each individual function has a strong dependence on the magnitude limit of the sub-sample

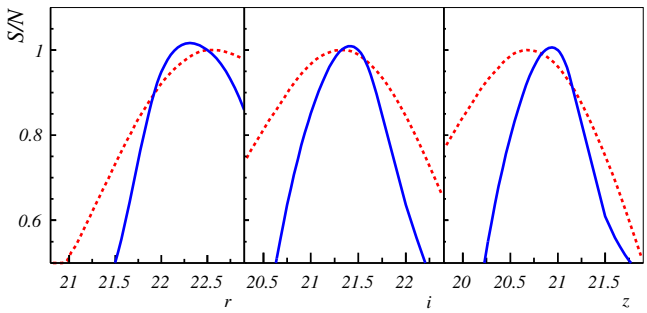

Figure 6. Red dashed line: expected signal-to-noise ratio computed with Equation 16. Blue solid line is the measured significance of the data. Both curves are normalized to their respective maximum.

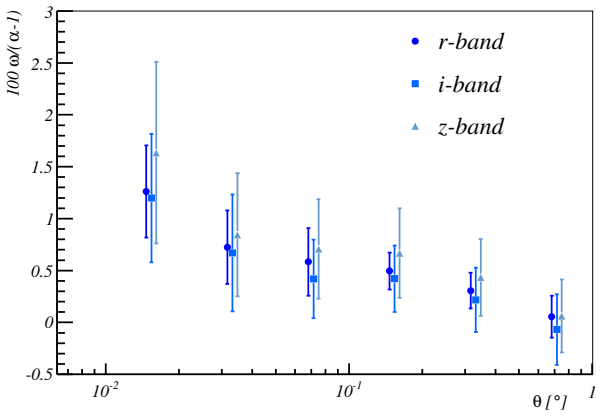

Figure 7. Example of the achromaticity of the measured signal. Here are shown the measured two-point angular cross-correlation functions for $r < 22.5$, $i < 22.0$ and $z < 21.5$ divided by their corresponding $\alpha - 1$.

considered, being always below the 3σ significance level. At the bright cuts, shot-noise prevents the identification of a non-zero magnification signal. At the faint end, although the sub-samples are much more populated, the strength of the magnification signal is nearly zero. This behavior has been compared with the one predicted at section 3. Predicted and measured values are plotted together in Figure 6. It can be seen that the location of the maximum signal-to-noise is predicted accurately.

When using the full covariance, computed one per each band, an improvement on the significance of detection is obtained, reaching a 3.5σ level of significance on each of the three bands, allowing us to claim that a signal for magnification has been detected.

A usual approach to enhance the signal-to-noise ratio, is to define an unique source sample and weight each source galaxy with its corresponding $(\alpha_S(m) - 1)^2$ value (Scranton et al. 2005). This weighted sum of galaxies enhances the significance of the measured signal by summing coherently positive and negative signals (instead of averaging them) and downweighting those with zero amplitude. Nevertheless, since no negative values of the number count can be measured with these samples, no improvement is made with the weighed sum.

Finally, in order to test that the signal is achromatic, that is, its strength is independent of the considered band, the measured two-point angular cross-correlation functions are divided by their corresponding number count slope parameter and comparisons are made among them. All cross-correlation functions fluctuate within 1σ errors (see Figure 7 for an example) demonstrating that the measured convergence field does not depend on the considered band.

6.2 Systematic errors

Here, the impact of potential sources of systematic errors on the measured two-point angular cross-correlation function is investigated and how they are taken into account in the measurement is described.

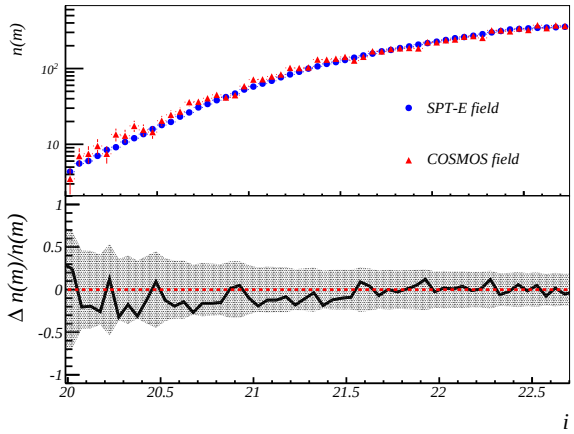

Figure 8. Upper panel: Comparison of the magnitude distribution for the SPT-E and the COSMOS fields. Both histograms are normalized by their respective area. Lower panel: Relative difference between the magnitude distribution of the COSMOS and the SPT-E fields. The shaded region shows the 1σ confidence interval computed from shot-noise.

6.2.1 *Number count slope α*

When comparing the measured two point angular cross-correlation functions with the theoretical prediction via Equation 15 for a given set of cosmological parameters, $\alpha(m)$ is determined by fitting the cumulative number count distribution to Equation 23 and then using Equation 9. To compute the possible impact of the uncertainty of this fit on the comparison with theory, a marginalization over all the parameters of fit (A, m_*, β) is made.

Assuming that the parameters are independent, they are randomly sampled with a Gaussian distribution centered on the value given by the fit to the cumulative number count and with a standard deviation equal to the 1σ errors of the fit. The value of α is recalculated with these randomly sampled parameters. The impact of the dispersion of

the α values obtained is negligible compared to the size of the jackknife errors, so they are not taken into account.

In addition to the parameter determination, a possible non-completeness on the SPT-E field can modify the magnitude distribution altering the cumulative number count slope parameter (Hildebrandt 2016). To estimate the possible impact of non-completeness, the measured magnitude distributions of the SPT-E field are compared with those of deeper fields measured by DES, such as the COSMOS field. Both distributions are found to be equal at the range of magnitudes considered on this analysis (see Figure 8 for an example in the i-band).

6.2.2 Object obscuration

Chang et al. (2015) studied whether moderately bright objects in crowded environments produce a decrease in the detection probability of nearby fainter objects at scales $\theta \lesssim 10$ arcsec. However, such scales are well below those considered in this analysis ($\theta > 36$ arcsec) and therefore this effect is ignored.

6.2.3 Stellar contamination

For a given choice of star-galaxy classifier, there will be a number of stars misclassified as galaxies, so the observed two-point angular cross-correlation function $\omega_O(\theta)$ must be corrected by the presence of any fake signal induced by stars (see appendix A):

$$\omega_{\mathrm{LS_j}} = \frac{\omega_{\mathrm{O}}(\theta) - \lambda_{\mathrm{L}}\omega_{*\mathrm{S_j}}(\theta) - \lambda_{\mathrm{S_j}}\omega_{\mathrm{L}*}(\theta)}{1 - \lambda_{\mathrm{L}} - \lambda_{\mathrm{S_j}}}, \tag{30}$$

where $\omega_{\mathrm{LS_j}}$ is the corrected galaxy cross-correlation function, $\omega_{\mathrm{L}*}$ is the cross-correlation function of the true galaxy lenses with the stars misclassified as galaxies in the source sample, $\omega_{*\mathrm{S_j}}$ is the cross correlation of the stars misclassified as galaxies in the lenses with the true source galaxies and $\lambda_{\mathrm{L}}, \lambda_{\mathrm{S_j}}$ are the fraction of stars in the lens and in the source samples respectively. Assuming that the misclassification of stars is spatially random and is a representative sample of the spatial distribution of the population classified as stars and that the fraction of misclassified stars is small, the functions $\omega_{\mathrm{L}*}, \omega_{*\mathrm{S_j}}$ are estimated from the cross-correlation of the galaxy population and the stellar population in the corresponding redshift bin.

Following a similar approach to Ross et al. (2012), if the latter is true and the misclassified stars trace the global population of stars, for a given patch of the sky the number of objects classified as galaxies N_{O} must be the average number of true galaxies $\bar{N}_{\mathrm{g}}$ plus a quantity proportional to the number of stars on that given pixel,

$$N_{\mathrm{O}} = \bar{N}_{\mathrm{g}} + \tilde{\gamma} N_{\mathrm{s}}. \tag{31}$$

Dividing by the average number of objects marked as galaxies $\bar{N}_{\mathrm{O}}$,

$$\frac{N_{\mathrm{O}}}{\bar{N}_{\mathrm{O}}} = p + \gamma N_{\mathrm{s}}, \tag{32}$$

where $p = \bar{N}_{\mathrm{g}}/\bar{N}_{\mathrm{O}}$ is the purity of the sample, that is, $\lambda = 1 - p$.

In order to estimate the purity of the galaxy sample

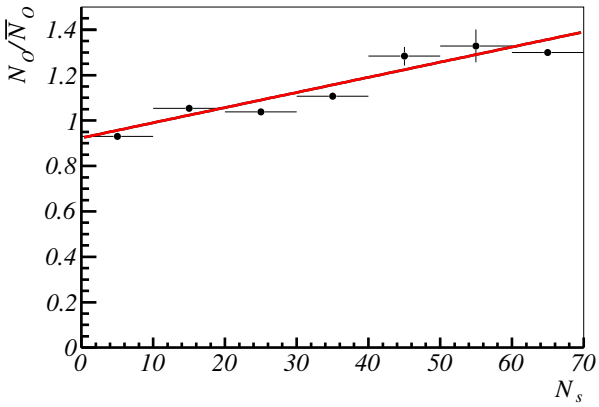

Figure 9. Determination of the purity of the lens sample. For each $N_{\mathrm{nside}} = 512$ HEALPix-pixel, the number of objects classified as galaxies divided by the average number of galaxies per pixel is plotted as a function of the number of objects classified as stars. Black dots are the measured data. Red line is the linear fit to the data. The intercept of the line with the Y-axis is the estimated purity of the sample.

with this method, an $N_{\mathrm{side}} = 512$ HEALPix pixelation is made and for each pixel $N_{\mathrm{O}}/\bar{N}_{\mathrm{O}}$ and N_{s} is computed. Then, a fit to Equation 32 is made determining a purity of 94 per cent for the lens sample and about 98 per cent for the source sample depending on the considered band (see Figure 9 for an example). With this purity, the correction due to stellar contamination given by Equation 30 is found to be one order of magnitude smaller than the statistical errors (see Figure 10 for the i-band correction), so stellar contamination is not taken into account in the analysis. Nevertheless, on future analysis with more galaxies and area this may be important. Note that the objects labeled as stars by our star-galaxy classifier would be a combination of stars and galaxies thus these calculations are an upper bound to stellar contamination.

6.2.4 Survey observing conditions

Observing conditions are not constant during the survey, leading to spatial dependencies across the DES-SV footprint (Leistedt et al. 2015) that may affect the observed cross-correlation function, such as seeing variations, air-mass, sky-brightness or exposure time (Morrison & Hildebrandt 2015). To trace these spatial variations, the 'simulated injection' Balrog catalog has been used as random sample (Suchyta et al. 2016). It is important to remark that Balrog catalogs are produced with the same pipeline as DES-SV data, allowing one to trace subtle effects such as patchiness on the zeropoints, deblending and possible magnitude errors due to a wrong sky subtraction close to bright objects.

6.2.5 Dust extinction

The possible presence of dust in the lenses may modify the observed magnitude in addition to the magnitude shift due

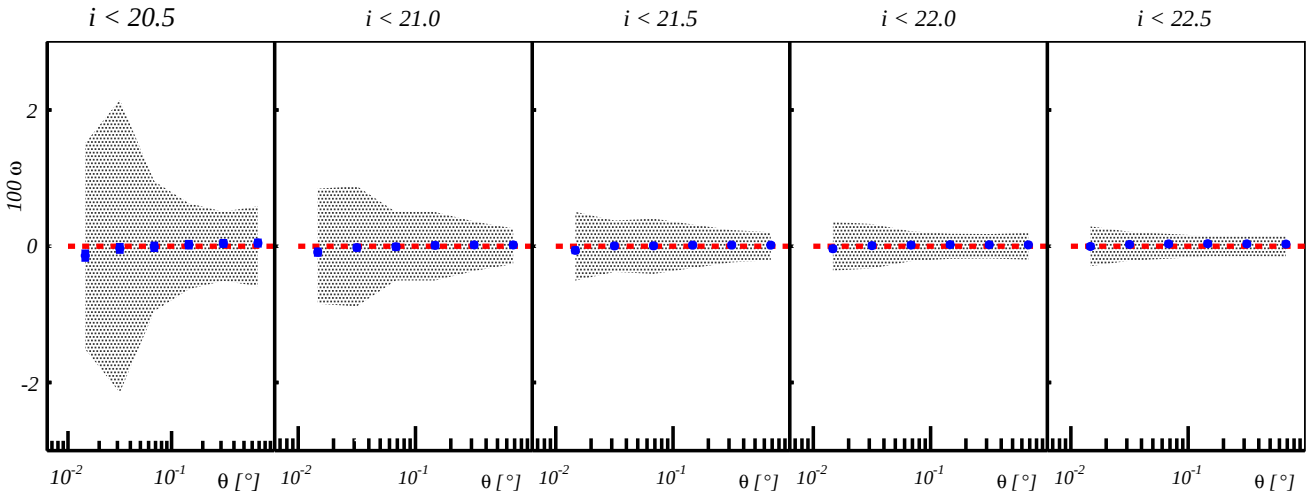

Figure 10. Correction by stellar contamination on the i-band sample. Blue dots are the correction and shaded area is the 1σ confidence interval of the measured cross-correlations of the magnification signal. Red dashed line is and eye-guide for zero.

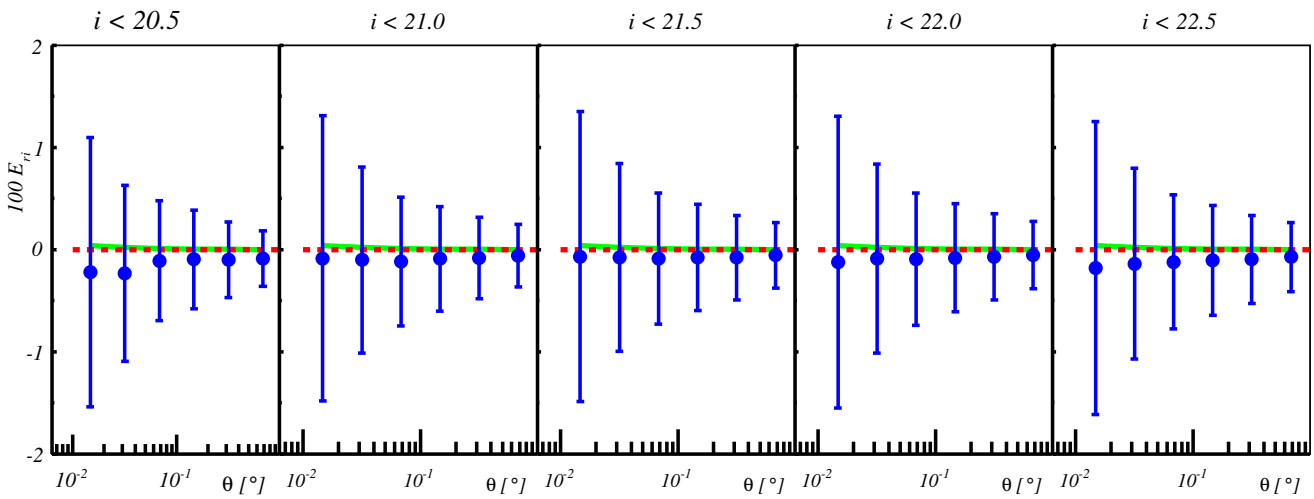

Figure 11. Blue dots: color-density cross-correlation functions measured on SV data for the r and i bands. Green solid line is the expected value from Equation 36. Red dashed line is an eye-guide for zero.

to magnification (Ménard et al. 2010). The change in magnitude (δm) on the p-band may be written as

$$\delta m_p = -2.5 \log \mu + \frac{2.5}{\ln 10} \tau_p, \tag{33}$$

where $\mu \simeq 1 + 2\kappa$ is the change in magnitude due to magnification and τ_k is the optical depth due to dust extinction. Whereas magnification is achromatic, dust extinction induces a band-dependent magnitude change. Taking this into account, the color-excess for bands p, q[9] is defined as

$$E_{pq} = \delta m_p - \delta m_q = 1.08[\tau_p - \tau_q]. \tag{34}$$

[9] In this section p, q stand for a generic index label while V stands for the V band of the UBV system.

Define the color-density cross-correlation as (Ménard et al. 2010)

$$\langle \delta_{\rm g} E_{pq} \rangle(\theta) = 1.09[\tau_p(\theta) - \tau_q(\theta)], \tag{35}$$

where $\delta_{\rm g}$ is the density contrast of the lenses and E_{pq} is the color-excess of the sources; from the measurements by Ménard et al. (2010) it can be parametrized as

$$\langle \delta_{\rm g} E_{pq} \rangle(\theta) = 1.09 \tau_V \left[\frac{\lambda_V}{\lambda_p} - \frac{\lambda_V}{\lambda_q} \right] \left(\frac{\theta}{1'} \right)^{-0.8}, \tag{36}$$

with $\tau_V = 2.3 \times 10^{-3}$ the optical depth at the V-band and $\lambda_V, \lambda_p, \lambda_q$ the average wavelengths of the V, p and q bands respectively. With this parametrization, the impact of dust extinction is negligible at the scales considered on this analysis. As it can be seen in Figure 11, color-density cross-

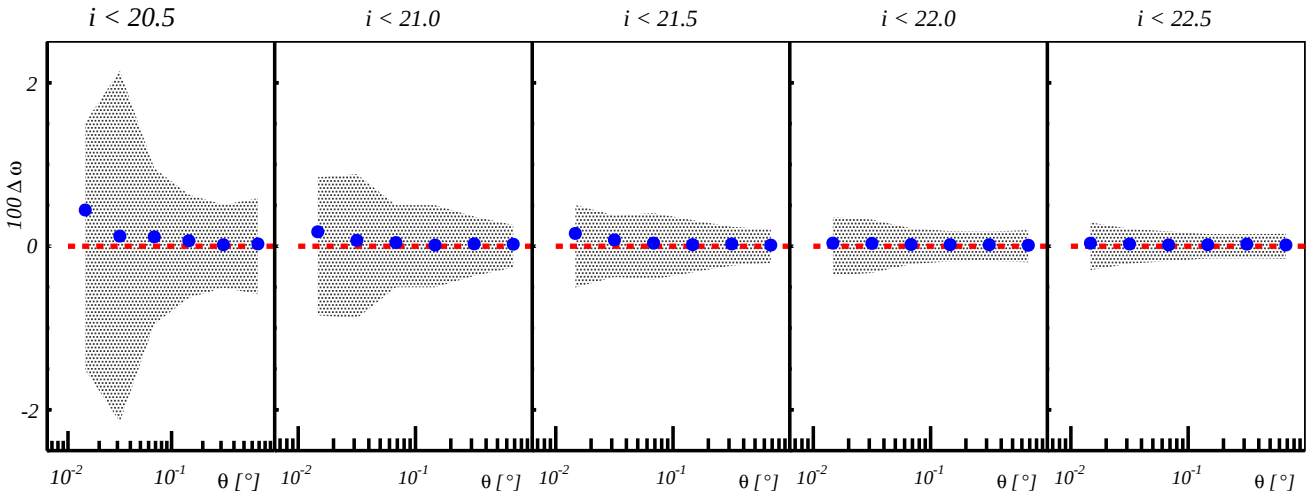

Figure 12. Impact of dust on the number count from MICE. Shade is the 1σ confidence interval. Blue dots are the number count differences between the case with and the case without the simulated dust profile. Red dashed line is an eye-guide for zero.

correlation functions are compatible with Equation 36 as well as with zero.

In addition, the impact of a dust profile has been simulated as described in Equation 36 with the MICE simulation (section 5). To do so, for each galaxy belonging to the source sample a magnitude shift is induced

$$m_d = m_\mu + 1.09\tau_V \frac{\lambda_V}{\lambda} \sum_l \left(\frac{\theta_l}{1'}\right)^{-0.8}. \qquad (37)$$

Here θ_l is the angular separation of the source-galaxy and the l-th lens galaxy and the summation is over all the galaxies of the lens sample. In Figure 12 the difference between the two-point angular cross-correlation with and without the dust can be seen to be less than the statistical errors. It can be deduced that dust has no impact on the angular scales considered on this work.

Since the parametrization used here only applies to a sample similar to the one used at Ménard et al. (2010), statements about dust constrains are limited. Nevertheless this does not change the fact that no chromatic effects are detected.

6.2.6 *Photometric redshifts*

A general study of photo-z performance in DES-SV can be found in Sánchez et al. (2014). A comprehensive study of the photo-z performance and its implications for weak lensing for this data can be found in Bonnett et al. (2016). Both studies are followed in this analysis. Conservative photo-z cuts are made in order to minimize migration between lens and source samples. Nevertheless, catastrophic outliers in the photo-z determination can bias the measurement of κ (Bernstein & Huterer 2010). Thus, the tails of the probability density functions (pdfs) of the photo-z code are a crucial systematic to test. As mentioned in section 2, in addition to the magnification signal, galaxy migration due to a wrong photo-z assignment between lens and source samples may induce a non-zero cross-correlation signal due to the physical signal coming from the clustering of objects in the same redshift bin. As a first approach, estimation of the expected signal induced by photo-z migration (ω^{ph}) is computed with Equation 13a:

$$\omega^{\rm ph}_{\rm LS_j}(\theta) = \int_0^\infty dz \int_0^\infty dz' \phi_{\rm L}(z)\phi_{\rm S_j}(z')\xi(\theta; z, z'), \qquad (38)$$

where $\xi(\theta; z, z')$ is the 3D correlation-function and $\phi_{\rm L}, \phi_{\rm S_j}$ are the redshift distribution of the lens (L) sample and the source sample ($\rm S_j$) estimated from the stacking of the pdfs given by TPZ. Figure 13 compares the measured two-point angular cross-correlation and the expected signal induced by photo-z can be seen for the I sample. The signal induced by photo-z is found to be smaller than the statistical errors. Note that this method relies on an assumed cosmology and bias model, and therefore should be considered only an approximation.

A more accurate calculation can be made with the help of N-body simulations. From the integration of the stacking of the pdfs it is found that the total photo-z migration between lens and source sample is $\sim 0.6\%$ depending on the magnitude cut of the source sample. To estimate the maximum photo-z migration allowed between the lens and the source sample, the MICE simulation (section 5) with the un-lensed coordinates and magnitudes is used. Galaxies are randomly sampled on the lens redshift bin and then placed on the source redshift bin. Conversely, galaxies on the source redshift bin are randomly sampled and placed on the lens redshift bin. For a given lens or source sample, the number of galaxies introduced from the other redshift bin is chosen to be 0.1, 0.3, 0.5, 0.7, 0.9 and 2 per cent of the galaxies. Then, the two-point angular cross-correlation is computed for each case. The difference of the correlation functions measured at the simulation with induced migration between lens and source sample and the original used at section 5 is the signal induced by photo-z migration. The signal induced by photo-z for the cases with 0.9 and 2 per cent computed with this method can be seen at Figure 14. It is found that at 0.9 per cent of contamination, the induced

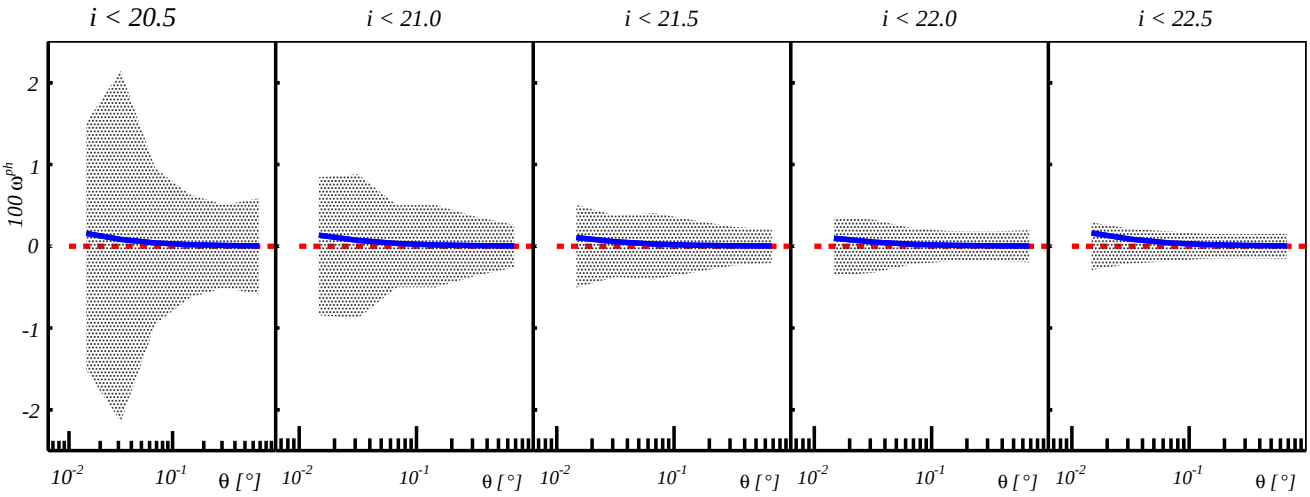

Figure 13. Comparison of 1σ jackknife errors of the measured correlation function (gray shade) with the expected signal induced by the photo-z migration between the lens and the source sample computed theoretically with the stacking of the pdfs for the i-band (blue line).

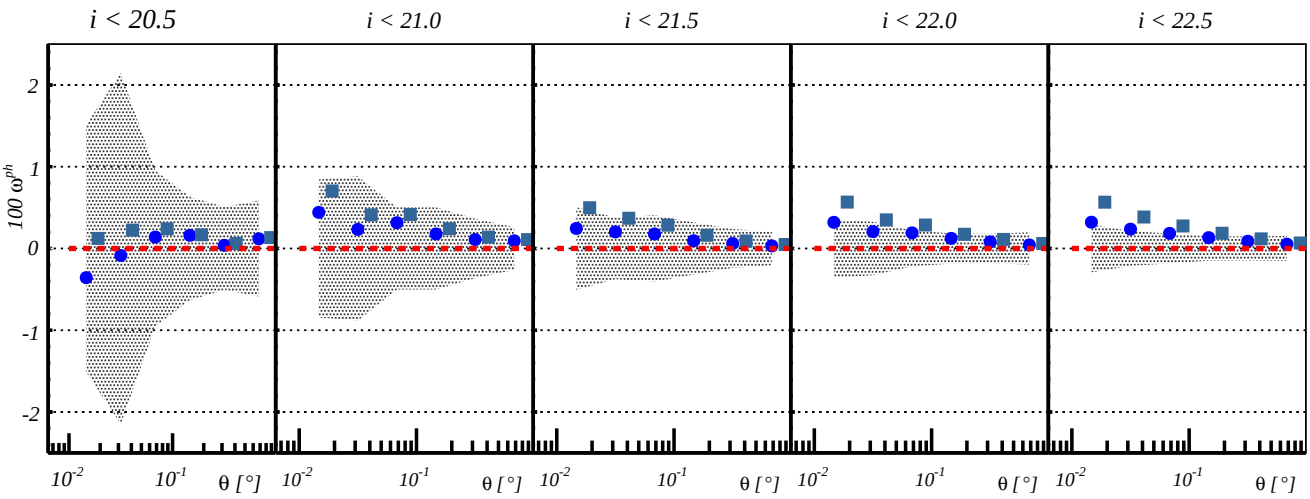

Figure 14. Estimation of the signal induced by migration of selected fractions of MICE un-lensed galaxies between the lens and the source sample. Shaded area is the 1σ confidence interval for the measured number count cross-correlations. Dark blue dots correspond to a contamination fraction of 0.9 per cent. Light blue squares correspond to a 2 per cent. Squares are displaced at the X axis for clarity. Red dashed line is an eye-guide for zero.

signal due to photo-z migration is comparable to the error in the correlation functions. This upper limit is greater than the estimated photo-z migration, demonstrating that the effect of photo-z migration is negligible. Photo-z migration has a larger impact on the brightest samples. Nevertheless, since the errors of the correlation functions of these samples are shot-noise dominated, the tightest constrains on photo-z migration are imposed by the faintest samples. With a larger data sample this statement will no longer be true.

Photo-z induced correlation functions that mimic magnification may affect the measured significance. Thus, Bayes factor is recomputed with two new hypothesis, the measured signal is a combination of magnification and photo-z $(M + Ph)$ or the measured signal is only photo-z (Ph):

$$\mathcal{K} = \frac{P(M + Ph|\Theta)}{P(Ph|\Theta)} = \frac{P(\Theta|M + Ph)}{P(\Theta|Ph)}, \tag{39}$$

where

$$P(\Theta|M + Ph) = e^{-\chi^2_{\rm Planck+Ph}/2} \tag{40}$$

and

$$P(\Theta|Ph) = e^{-\chi^2_{\rm Ph}/2}. \tag{41}$$

To compute $\chi^2_{\rm Planck+Ph}$ and $\chi^2_{\rm Ph}$ it has been assumed that the expected theory is given by $\omega_{\rm LS_j}(\theta) + \omega^{\rm ph}_{\rm LS_j}(\theta)$ and $\omega^{\rm ph}_{\rm LS_j}$ respectively, where $\omega^{\rm ph}_{\rm LS_j}$ is the expected signal induced by

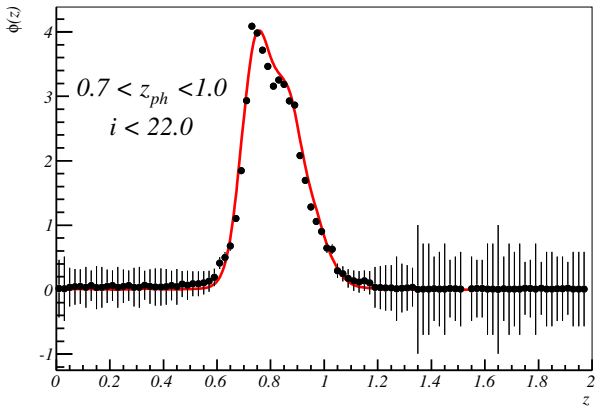

Figure 15. Comparison of the redshift distribution computed by the stacking of the pdfs given by TPZ (red solid line) with the ones computed with the spectroscopic sample (black dots).

photo-z computed using Equation 38. The significances re-computed using these two new hypothesis for the r, i and z bands are 2.7σ, 3.4σ and 3.5σ respectively. Thus, it can be concluded that photo-z migration has a limited impact on the measured significiances.

All previous calculations were based on the assumption that the pdfs are a reliable description of the true redshift distribution. This statement can be partially validated comparing the pdfs with the spectroscopic redshift distribution for the same sample (see Figure 15 for an example). Redshift distributions predicted by TPZ are found to be representative of those given by the spectroscopic sample. Nevertheless, this statement has limitations –but is good enough for SV data– and a more accurate description of the real redshift distribution of the full sample will be measured with methodologies involving clustering-based estimators (Newman (2008); Matthews & Newman (2010); Ménard et al. (2013); Scottez et al. (2016)) when the size of the data sample grows. This type of estimators involve the use of two-point angular cross-correlations between different redshift bins, whose measurement may be biased by number count magnification itself. Nevertheless, as it has been stated at section 2, depending on the value of the number count slope, the amplitude induced by magnification on the correlation-function may be zero. Thus, when employing this kind of estimators, samples should be carefully chosen so that $\alpha_S - 1 = 0$. This can be done by measuring the number count slope at the cumulative magnitude distribution with methods such that used in this work.

Finally, to demonstrate that the measured signal is independent of the photo-z technique employed to estimate the redshift, the two-point angular cross-correlation functions used on this analysis are re-computed with redshift estimated with other two different approaches that have shown to have similar performance as TPZ (Sánchez et al. 2014) a neural network, Skynet (Graff et al. 2014), and a template based approach, Bayesian Photo-Z (BPZ; Benítez (2000)). Figure 16 compares the cross-correlations computed with the three codes for the i-band, showing them to be within 1σ errors.

7 CONCLUSIONS

In this paper weak lensing magnification of number count has been detected for the first time with the Dark Energy Survey, reaching a significance level of 3.5σ on each of the r, i, z photometric bands. The measured magnification signal agrees with theoretical predictions using a ΛCDM model with Planck Collaboration et al. (2015) best-fit parameters.

This magnification measurement has been made on a purely photo-z selected sample of regular galaxies. In addition a criterion for signal-to-noise maximization has been described allowing us to have an objective criteria for sample selection on magnification analysis.

Systematic effects have been studied in detail not only using the data itself, but also supported with the N-body simulation MICE and the Balrog 'simulated injection'. Due to the limited size of the data sample, whose statistics are still dominated by shot noise, the only relevant systematic effect is the variation of the observing conditions across the footprint, a feature that was mitigated with the use of Balrog catalogs. The use of these catalogs, will allow us in the future to exploit the full depth of the survey (Suchyta et al. 2016).

A conservative photo-z selection avoided systematic effects on the measured magnification signal due to photo-z migration. Nevertheless, given the precision in photo-z, only one pair of lens-source redshift-bins could be considered. In future analysis this could be improved by selecting bright high-redshift objects such as quasars or Lyman break galaxies. This would allow us to define several lens bins and do a tomographic analysis (Morrison et al. 2012).

The detection of magnification has been made only with 3 per cent of the final planned area for DES and half of the available maximum depth. This demonstrates that magnification measurements are feasible in the Dark Energy Survey and will be a powerful cosmological tool.

Future work will include the analysis of DES observations in much wider area, where some of the systematic issues not significant here such as stellar contamination and the accurate determination of the number count slope parameter, may not be negligible. These analyses will include measurements of cosmological parameters –by themselves or in combination with other weak lensing measurements (van Waerbeke 2010)–, but also the other two effects of magnification: the observed magnitude shift (Ménard et al. 2010) and the increase in the observed size (Huff & Graves 2014).

ACKNOWLEDGEMENTS

We are grateful for the extraordinary contributions of our CTIO colleagues and the DECam Construction, Commissioning and Science Verification teams in achieving the excellent instrument and telescope conditions that have made this work possible. The success of this project also relies critically on the expertise and dedication of the DES Data Management group.

Funding for the DES Projects has been provided by the U.S. Department of Energy, the U.S. National Science Foundation, the Ministry of Science and Education of Spain, the Science and Technology Facilities Council of the United Kingdom, the Higher Education Funding Council for

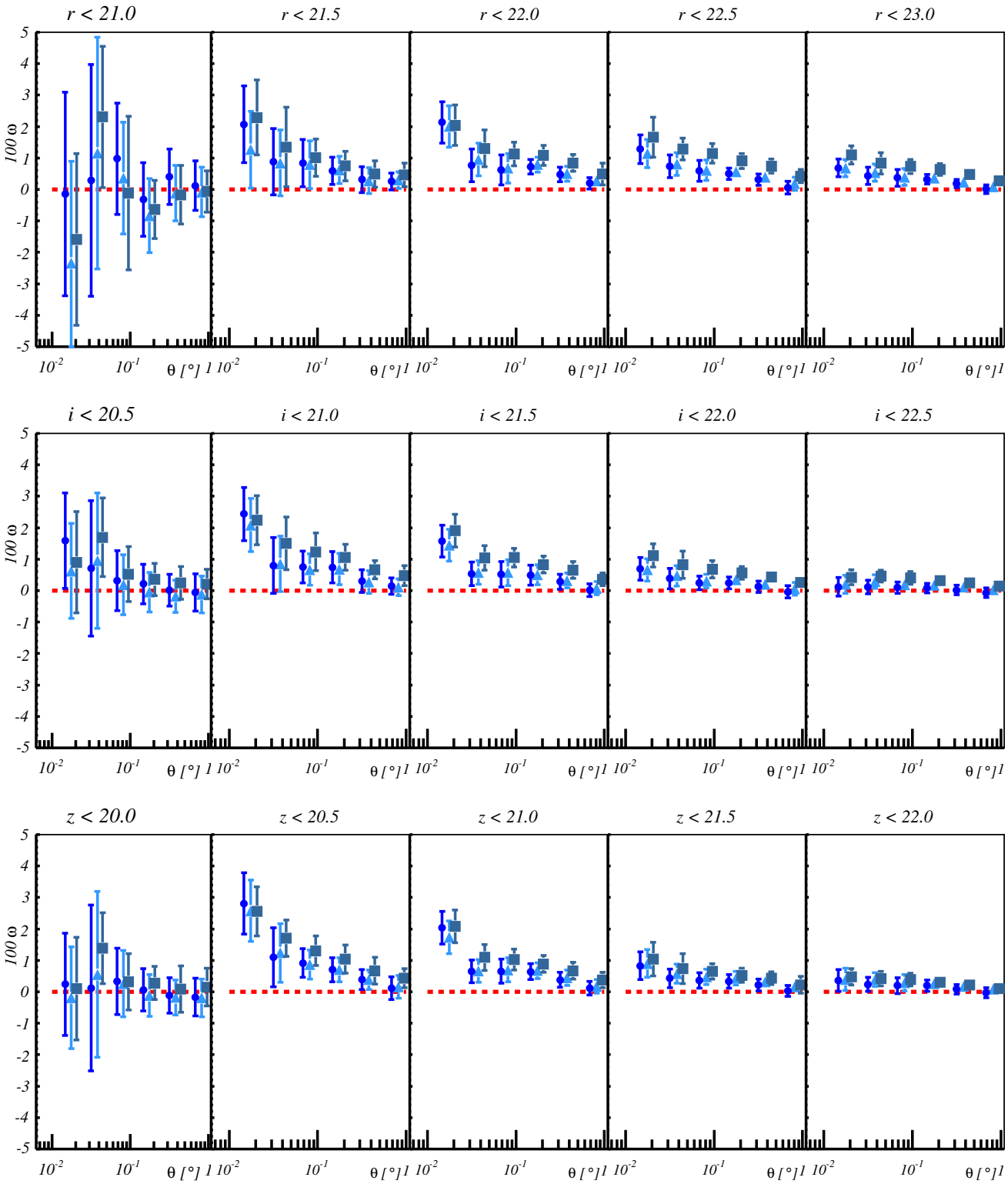

Figure 16. Comparison of the measured two-point angular cross-correlation functions measured with the Landy-Szalay estimator using TPZ (dark blue dots), Skynet (medium blue triangles) and BPZ (light blue squares). Triangles and squares are displaced at the horizontal axis for clarity. Red dashed line is an eye-guide for zero.

England, the National Center for Supercomputing Applications at the University of Illinois at Urbana-Champaign, the Kavli Institute of Cosmological Physics at the University of Chicago, the Center for Cosmology and Astro-Particle Physics at the Ohio State University, the Mitchell Institute for Fundamental Physics and Astronomy at Texas A&M University, Financiadora de Estudos e Projetos, Fundação Carlos Chagas Filho de Amparo à Pesquisa do Estado do Rio de Janeiro, Conselho Nacional de Desenvolvimento Científico e Tecnológico and the Ministério da Ciência, Tecnologia e Inovação, the Deutsche Forschungsgemeinschaft and the Collaborating Institutions in the Dark Energy Survey.

The Collaborating Institutions are Argonne National Laboratory, the University of California at Santa Cruz, the University of Cambridge, Centro de Investigaciones Energéticas, Medioambientales y Tecnológicas-Madrid, the University of Chicago, University College London, the DES-Brazil Consortium, the University of Edinburgh, the Eidgenössische Technische Hochschule (ETH) Zürich, Fermi National Accelerator Laboratory, the University of Illinois at Urbana-Champaign, the Institut de Ciències de l'Espai (IEEC/CSIC), the Institut de Física d'Altes Energies, Lawrence Berkeley National Laboratory, the Ludwig-Maximilians Universität München and the associated Excellence Cluster Universe, the University of Michigan, the National Optical Astronomy Observatory, the University of Nottingham, The Ohio State University, the University of Pennsylvania, the University of Portsmouth, SLAC National Accelerator Laboratory, Stanford University, the University of Sussex, and Texas A&M University.

The DES data management system is supported by the National Science Foundation under Grant Number AST-1138766.

The DES participants from Spanish institutions are partially supported by MINECO under grants AYA2012-39559, ESP2013-48274, FPA2015-68048, and Centro de Excelencia Severo Ochoa SEV-2012-0234 and María de Maeztu MDM-2015-0509. Research leading to these results has received funding from the European Research Council under the European Unions Seventh Framework Programme (FP7/2007-2013) including ERC grant agreements 240672, 291329, and 306478.

REFERENCES

Bartelmann M., 1992a, in Klare G., ed., Reviews in Modern Astronomy Vol. 5, Reviews in Modern Astronomy. pp 259–270
Bartelmann M., 1992b, Sterne und Weltraum, 31, 459
Bartelmann M., 1992c, in Kayser R., Schramm T., Nieser L., eds, Lecture Notes in Physics, Berlin Springer Verlag Vol. 406, Gravitational Lenses. p. 345, doi:10.1007/3-540-55797-0˙122
Bartelmann M., 1995a, A&A, 298, 661
Bartelmann M., 1995b, A&A, 303, 643
Bartelmann M., Narayan R., 1995, in Holt S. S., Bennett C. L., eds, American Institute of Physics Conference Series Vol. 336, Dark Matter. pp 307–319 (arXiv:astro-ph/9411033), doi:10.1063/1.48350
Bartelmann M., Schneider P., 1992, A&A, 259, 413
Bartelmann M., Schneider P., 1993, A&A, 268, 1
Bartelmann M., Schneider P., 2001, Phys. Rep., 340, 291
Bauer A. H., Gaztañaga E., Martí P., Miquel R., 2014, MNRAS, 440, 3701
Benítez N., 2000, ApJ, 536, 571
Bernstein G., Huterer D., 2010, MNRAS, 401, 1399
Bertin E., Arnouts S., 1996, A&AS, 117, 393
Blandford R. D., Narayan R., 1992, ARA&A, 30, 311
Blandford R. D., Kochanek C. S., Kovner I., Narayan R., 1989, Science, 245, 824
Bonnett C., et al., 2016, Phys. Rev. D, 94, 042005
Broadhurst T., 1995, in Holt S. S., Bennett C. L., eds, American Institute of Physics Conference Series Vol. 336, Dark Matter. pp 320–329 (arXiv:astro-ph/9505010), doi:10.1063/1.48351
Carrasco Kind M., Brunner R. J., 2013, MNRAS, 432, 1483
Chang C., et al., 2015, The Astrophysical Journal, 801, 73
Chiu I., et al., 2016, MNRAS, 457, 3050
Clerkin L., Kirk D., Lahav O., Abdalla F. B., Gaztañaga E., 2015, MNRAS, 448, 1389
Crocce M., Castander F. J., Gaztañaga E., Fosalba P., Carretero J., 2015, MNRAS, 453, 1513
Crocce M., et al., 2016, MNRAS, 455, 4301
Desai S., et al., 2012, ApJ, 757, 83
Diehl T., 2012, Physics Procedia, 37, 1332
Flaugher B., 2005, International Journal of Modern Physics A, 20, 3121
Flaugher B., et al., 2015, AJ, 150, 150
Ford J., Hildebrandt H., Van Waerbeke L., Erben T., Laigle C., Milkeraitis M., Morrison C. B., 2014, MNRAS, 439, 3755
Fosalba P., Gaztañaga E., Castander F. J., Crocce M., 2015a, MNRAS, 447, 1319
Fosalba P., Crocce M., Gaztañaga E., Castander F. J., 2015b, MNRAS, 448, 2987
Fugmann W., 1990, A&A, 240, 11
Gaztañaga E., 2003, The Astrophysical Journal, 589, 82
Górski K. M., Hivon E., Banday A. J., Wandelt B. D., Hansen F. K., Reinecke M., Bartelmann M., 2005, ApJ, 622, 759
Graff P., Feroz F., Hobson M. P., Lasenby A., 2014, MNRAS, 441, 1741
Grossman S. A., Narayan R., 1989, ApJ, 344, 637
Hildebrandt H., 2016, MNRAS, 455, 3943
Hoekstra H., Jain B., 2008, Annual Review of Nuclear and Particle Science, 58, 99
Hogan C. J., Narayan R., White S. D. M., 1989, Nature, 339, 106
Huff E. M., Graves G. J., 2014, The Astrophysical Journal Letters, 780, L16
Hui L., Gaztañaga E., LoVerde M., 2007, Phys. Rev. D, 76, 103502
Hui L., Gaztañaga E., LoVerde M., 2008, Phys. Rev. D, 77, 063526
Jain B., Lima M., 2011, MNRAS, 411, 2113
Jarvis M., Bernstein G., Jain B., 2004, MNRAS, 352, 338
Kaiser N., 1984, ApJ, 284, L9
Kilbinger M., 2015, Reports on Progress in Physics, 78, 086901
Landy S. D., Szalay A. S., 1993, ApJ, 412, 64
Leistedt B., et al., 2015, preprint, (arXiv:1507.05647)
LoVerde M., Hui L., Gaztañaga E., 2008, Phys. Rev. D, 77, 023512
MacQueen J., et al., 1967, in Proceedings of the fifth Berkeley symposium on mathematical statistics and probability. pp 281–297
Mandelbaum R., et al., 2005, MNRAS, 361, 1287
Matthews D. J., Newman J. A., 2010, ApJ, 721, 456
Ménard B., Bartelmann M., 2002, A&A, 386, 784
Ménard B., Hamana T., Bartelmann M., Yoshida N., 2003, A&A, 403, 817
Ménard B., Scranton R., Fukugita M., Richards G., 2010, MNRAS, 405, 1025
Ménard B., Scranton R., Schmidt S., Morrison C., Jeong D., Budavari T., Rahman M., 2013, preprint, (arXiv:1303.4722)
Meylan G., Jetzer P., North P., Schneider P., Kochanek C. S., Wambsganss J., eds, 2006, Gravitational Lensing: Strong, Weak and Micro (arXiv:astro-ph/0407232)
Moessner R., Jain B., 1998, MNRAS, 294, L18
Mohr J. J., et al., 2012, in Software and Cyberinfrastruc-

ture for Astronomy II. p. 84510D (arXiv:1207.3189), doi:10.1117/12.926785
Morrison C. B., Hildebrandt H., 2015, MNRAS, 454, 3121
Morrison C. B., Scranton R., Ménard B., Schmidt S. J., Tyson J. A., Ryan R., Choi A., Wittman D. M., 2012, MNRAS, 426, 2489
Narayan R., 1989, ApJ, 339, L53
Narayan R., Wallington S., 1993, in Surdej J., Fraipont-Caro D., Gosset E., Refsdal S., Remy M., eds, Liege International Astrophysical Colloquia Vol. 31, Liege International Astrophysical Colloquia. p. 217
Newman J. A., 2008, ApJ, 684, 88
Peacock J. A., Dodds S. J., 1994, MNRAS, 267, 1020
Pedregosa F., et al., 2011, Journal of Machine Learning Research, 12, 2825
Planck Collaboration et al., 2015, preprint, (arXiv:1502.01589)
Ross A. J., et al., 2012, MNRAS, 424, 564
Sánchez C., et al., 2014, MNRAS, 445, 1482
Schechter P., 1976, ApJ, 203, 297
Scottez V., et al., 2016, MNRAS, 462, 1683
Scranton R., et al., 2005, The Astrophysical Journal, 633, 589
Seldner M., Peebles P. J. E., 1979, ApJ, 227, 30
Sevilla I., et al., 2011, preprint, (arXiv:1109.6741)
Suchyta E., et al., 2016, MNRAS, 457, 786
Swanson M. E. C., Tegmark M., Hamilton A. J. S., Hill J. C., 2008, MNRAS, 387, 1391
Weinberg D. H., Mortonson M. J., Eisenstein D. J., Hirata C., Riess A. G., Rozo E., 2013, Physics Reports, 530, 87
White S. D. M., Rees M. J., 1978, MNRAS, 183, 341
van Waerbeke L., 2010, MNRAS, 401, 2093
van Waerbeke L., Hildebrandt H., Ford J., Milkeraitis M., 2010, The Astrophysical Journal Letters, 723, L13

APPENDIX A: INFLUENCE OF STELLAR CONTAMINATION ON THE TWO-POINT ANGULAR CROSS-CORRELATION

The observed density contrast of objects is given by

$$\delta_{\rm O}(\hat{\boldsymbol{n}}, z_i) = \frac{N_{\rm g}(z_i) + N_*(z_i)}{\bar{N}_{\rm g}(z_i) + \bar{N}_*(z_i)} - 1, \quad \text{(A1)}$$

where $N_{\rm g}, N_*$ are the number of galaxies on direction $\hat{\boldsymbol{n}}$ and redshift z_i and stars respectively and $\bar{N}_{\rm g}, \bar{N}_*$ the average number of galaxies and stars over the footprint. The previous equation can be expressed as

$$\delta_{\rm O}(\hat{\boldsymbol{n}}, z_i) = \frac{N_{\rm g}(z_i) + N_*(z_i)}{\bar{N}_{\rm g}(z_i)\left[1 + \frac{\bar{N}_*(z_i)}{\bar{N}_{\rm g}(z_i)}\right]} - 1. \quad \text{(A2)}$$

Taylor expanding the brackets one has,

$$\delta_{\rm O}(\hat{\boldsymbol{n}}, z_i) = \frac{N_{\rm g}(z_i) + N_*(z_i)}{\bar{N}_{\rm g}(z_i)}\left[1 - \frac{\bar{N}_*(z_i)}{\bar{N}_{\rm g}(z_i)}\right] - 1 \quad \text{(A3)}$$

and taking common factor $\bar{N}_*(z_i)/\bar{N}_{\rm g}(z_i)$,

$$\delta_{\rm O}(z_i) = \left[\frac{N_{\rm g}(z_i)}{\bar{N}_{\rm g}(z_i)} - 1\right] + \frac{\bar{N}_*(z_i)}{\bar{N}_{\rm g}(z_i)}\left[\frac{N_*(z_i)}{\bar{N}_*(z_i)} - \frac{N_{\rm g}(z_i)}{\bar{N}_{\rm g}(z_i)}\right] - \frac{N_*(z_i)}{\bar{N}_{\rm g}(z_i)}. \quad \text{(A4)}$$

Assuming that $\bar{N}_* \ll \bar{N}_g$, the last term can be neglected and defining $\lambda_i = \bar{N}_*(z_i)/\bar{N}_{\rm g}(z_i)$ as the fraction of stars on the i-th sample,

$$\delta_{\rm O}(\hat{\boldsymbol{n}}, z_i) = \delta_{\rm g}(\hat{\boldsymbol{n}}, z_i) + \lambda_i[\delta_*(\hat{\boldsymbol{n}}, z_i) - \delta_{\rm g}(\hat{\boldsymbol{n}}, z_i)]. \quad \text{(A5)}$$

Calculating the two point angular cross-correlation results finally in

$$\omega_{\rm O} = (1 - \lambda_i - \lambda_j)\omega_{\rm gg} + \lambda_j\omega_{\rm g*} + \lambda_i\omega_{*\rm g} + \lambda_i\lambda_j\omega_{**}. \quad \text{(A6)}$$

AFFILIATIONS

[1] Centro de Investigaciones Energéticas, Medioambientales y Tecnológicas (CIEMAT), Madrid, Spain
[2] Computer Science and Mathematics Division, Oak Ridge National Laboratory, Oak Ridge, TN 37831
[3] Jet Propulsion Laboratory, California Institute of Technology, 4800 Oak Grove Dr., Pasadena, CA 91109, USA
[4] Institut de Ciències de l'Espai, IEEC-CSIC, Campus UAB, Carrer de Can Magrans, s/n, 08193 Bellaterra, Barcelona, Spain
[5] Institut de Física d'Altes Energies (IFAE), The Barcelona Institute of Science and Technology, Campus UAB, 08193 Bellaterra (Barcelona) Spain
[6] Universitäts-Sternwarte, Fakultät für Physik, Ludwig-Maximilians Universität München, Scheinerstr. 1, 81679 München, Germany
[7] Cerro Tololo Inter-American Observatory, National Optical Astronomy Observatory, Casilla 603, La Serena, Chile
[8] Department of Physics & Astronomy, University College London, Gower Street, London, WC1E 6BT, UK
[9] Department of Physics and Electronics, Rhodes University, PO Box 94, Grahamstown, 6140, South Africa
[10] Fermi National Accelerator Laboratory, P. O. Box 500, Batavia, IL 60510, USA
[11] CNRS, UMR 7095, Institut d'Astrophysique de Paris, F-75014, Paris, France
[12] Sorbonne Universités, UPMC Univ Paris 06, UMR 7095, Institut d'Astrophysique de Paris, F-75014, Paris, France
[13] Department of Physics and Astronomy, University of Pennsylvania, Philadelphia, PA 19104, USA
[14] Kavli Institute for Particle Astrophysics & Cosmology, P. O. Box 2450, Stanford University, Stanford, CA 94305, USA
[15] SLAC National Accelerator Laboratory, Menlo Park, CA 94025, USA
[16] Laboratório Interinstitucional de e-Astronomia - LIneA, Rua Gal. José Cristino 77, Rio de Janeiro, RJ - 20921-400, Brazil
[17] Observatório Nacional, Rua Gal. José Cristino 77, Rio de Janeiro, RJ - 20921-400, Brazil
[18] Department of Astronomy, University of Illinois, 1002 W. Green Street, Urbana, IL 61801, USA
[19] National Center for Supercomputing Applications, 1205 West Clark St., Urbana, IL 61801, USA
[20] Institute of Cosmology & Gravitation, University of Portsmouth, Portsmouth, PO1 3FX, UK
[21] School of Physics and Astronomy, University of Southampton, Southampton, SO17 1BJ, UK
[22] George P. and Cynthia Woods Mitchell Institute for Fundamental Physics and Astronomy, and Department of Physics and Astronomy, Texas A&M University, College Station, TX 77843, USA
[23] Department of Physics, IIT Hyderabad, Kandi, Telangana 502285, India
[24] Department of Astronomy, University of Michigan, Ann

Arbor, MI 48109, USA
[25] Department of Physics, University of Michigan, Ann Arbor, MI 48109, USA
[26] Kavli Institute for Cosmological Physics, University of Chicago, Chicago, IL 60637, USA
[27] Instituto de Física Teórica IFT-UAM/CSIC Universidad Autónoma de Madrid, Cantoblanco 28049, Madrid, Spain
[28] Institute of Astronomy, University of Cambridge, Madingley Road, Cambridge CB3 0HA, UK
[29] Kavli Institute for Cosmology, University of Cambridge, Madingley Road, Cambridge CB3 0HA, UK
[30] Astronomy Department, University of Washington, Box 351580, Seattle, WA 98195, USA
[31] Australian Astronomical Observatory, North Ryde, NSW 2113, Australia
[32] Departamento de Física Matemática, Instituto de Física, Universidade de São Paulo, CP 66318, CEP 05314-970, São Paulo, SP, Brazil
[33] Jodrell Bank Center for Astrophysics, School of Physics and Astronomy, University of Manchester, Oxford Road, Manchester, M13 9PL, UK
[34] Department of Astrophysical Sciences, Princeton University, Peyton Hall, Princeton, NJ 08544, USA
[35] Institució Catalana de Recerca i Estudis Avançats, E-08010 Barcelona, Spain
[36] Excellence Cluster Universe, Boltzmannstr. 2, 85748 Garching, Germany
[37] Faculty of Physics, Ludwig-Maximilians-Universität, Scheinerstr. 1, 81679 Munich, Germany
[38] Max Planck Institute for Extraterrestrial Physics, Giessenbachstrasse, 85748 Garching, Germany
[39] Department of Physics and Astronomy, Pevensey Building, University of Sussex, Brighton, BN1 9QH, UK
[40] Universidade Federal do ABC, Centro de Ciências Naturais e Humanas, Av. dos Estados, 5001, Santo André, SP, Brazil, 09210-580

This paper has been typeset from a TEX/LATEX file prepared by the author.